

Five-parameter crystallographic characteristics of the interfaces formed during ferrite to austenite transformation in a duplex stainless steel

N. Haghdadi, P. Cizek, P. D. Hodgson, V. Tari, G. S. Rohrer & H. Beladi

To cite this article: N. Haghdadi, P. Cizek, P. D. Hodgson, V. Tari, G. S. Rohrer & H. Beladi (2018) Five-parameter crystallographic characteristics of the interfaces formed during ferrite to austenite transformation in a duplex stainless steel, Philosophical Magazine, 98:14, 1284-1306, DOI: [10.1080/14786435.2018.1434321](https://doi.org/10.1080/14786435.2018.1434321)

To link to this article: <https://doi.org/10.1080/14786435.2018.1434321>



Published online: 07 Feb 2018.



Submit your article to this journal [↗](#)



Article views: 67



View related articles [↗](#)



View Crossmark data [↗](#)



Five-parameter crystallographic characteristics of the interfaces formed during ferrite to austenite transformation in a duplex stainless steel

N. Haghdadi^a, P. Cizek^a, P. D. Hodgson^a, V. Tari^b, G. S. Rohrer^b and H. Beladi^a

^aInstitute for Frontier Materials, Deakin University, Waurn Ponds, Australia; ^bDepartment of Materials Science and Engineering, Carnegie Mellon University, Pittsburgh, PA, USA

ABSTRACT

The crystallography of interfaces in a duplex stainless steel having an equiaxed microstructure produced through the ferrite to austenite diffusive phase transformation has been studied. The five-parameter interface character distribution revealed a high anisotropy in habit planes for the austenite–ferrite and austenite–austenite interfaces for different lattice misorientations. The austenite and ferrite habit planes largely terminated on (1 1 1) and (1 1 0) planes, respectively, for the austenite–ferrite interfaces associated with Kurdjumov–Sachs (K–S) and Nishiyama–Wasserman (N–W) orientation relationships. This was mostly attributed to the crystallographic preference associated with the phase transformation. For the austenite–ferrite interfaces with orientation relationships which are neither K–S nor N–W, both austenite and ferrite habit planes had (1 1 1) orientations. $\Sigma 3$ twin boundaries comprised the majority of austenite–austenite interfaces, mostly showing a pure twist character and terminating on (1 1 1) planes due to the minimum energy configuration. The second highest populated austenite–austenite boundary was $\Sigma 9$, which tended to have grain boundary planes in the tilt zone due to the geometrical constraints. Furthermore, the intervariant crystallographic plane distribution associated with the K–S orientation relationship displayed a general tendency for the austenite habit planes to terminate with the (1 1 1) orientation, mainly due to the crystallographic preference associated with the phase transformation.

ARTICLE HISTORY

Received 11 August 2017
Accepted 29 November 2017

KEYWORDS

Interface plane distribution; habit plane; phase transformation; duplex stainless steel; texture

1. Introduction

Duplex stainless steels represent an important class of stainless steels with low-cost, excellent corrosion resistance, satisfying mechanical properties and good weldability [1]. These advantages lead to an ongoing quest to use this grade of

steels in diversified applications. Based on the phase diagram, these steels solidify as delta-ferrite, which partially transforms to austenite during cooling to room temperature. The microstructure is complex, as it consists of two distinct phases with different crystal structures and stacking fault energies. Consequently, there are different types of boundaries/interfaces in the microstructure, namely ferrite–ferrite, ferrite–austenite and austenite–austenite boundaries, which may affect a property of interest (such as precipitation [2], hot working [3] and fracture [4,5] behaviour) differently due to their distinct characteristics.

The austenite–ferrite interface characteristics significantly influence the material's plasticity. Micro-cracks are mostly initiated at ferrite–austenite interfaces having irrational crystallographic orientation relationships (OR) [6]. In fact, the transition of slip from one phase to the other becomes easier at interfaces having a rational OR (e.g. Kurdjumov–Sachs, K–S) due to the presence of common slip systems on either side of the interface [7]. This relieves the stress concentration at the interface, lowering the tendency for crack initiation. Austenite/ferrite interface sliding has also been reported to depend on the interface character. The rational interfaces exhibit higher resistance to sliding compared with their irrational counterparts [8,9]. The propensity for $(\text{Fe,Ni})_x(\text{Cr,Mo})_y$ σ phase precipitation is also affected by the interface characteristics, as the rational interfaces retard the precipitation significantly [2,10]. Since the characteristics of interfaces in duplex stainless steel control a wide range of properties such as precipitation [2,10], hot working [3] and fracture [4] behaviour, it is necessary to characterise different interfaces formed during phase transformation.

Past attempts to characterise ferrite–austenite interfaces in duplex stainless steels have used either transmission electron microscopy (TEM) [11,12] or electron back-scattered diffraction (EBSD) [13,14]. The former is restricted to a small number of interfaces due to a limited area of examination, so the statistical significance is questionable. The latter mostly characterised the interfaces based on the lattice misorientation and did not measure the distribution of interface plane orientations associated with these boundaries. Recently, a stereological analysis of EBSD data was used to characterise the boundary plane distribution for all of the interfaces formed in a hot rolled duplex stainless steel subjected to an annealing process [15]. This study, however, did not separately characterise the habit planes of austenite and ferrite for austenite–ferrite interfaces with different orientation relationships.

The aim of the current study was to characterise different types of interfaces formed through the ferrite to austenite phase transformation (i.e. ferrite–austenite and austenite–austenite) in a duplex stainless steel. All five independent crystallographic parameters of each interface, i.e. both the corresponding misorientation and boundary plane, have been extracted from the EBSD data using an automated stereological approach. For the ferrite–austenite interfaces, the habit planes of austenite and ferrite were determined separately for interphase interfaces associated with different orientation relationships [16]. In addition, a detailed analysis was

performed on different types of austenite–austenite interfaces formed through the phase transformation.

2. Experimental procedure

The experimental material was a 2205 duplex stainless steel with the chemical composition of 0.036 C, 0.321 Si, 1.82 Mn, 0.013 P, 23.2 Cr, 2.90 Mo, 5.6 Ni, 0.034 Co, 0.153 Cu, 0.018 Nb, 0.065 V, 0.025 W, 0.245 N (in wt. %) and remainder Fe. The as-received material was in the form of a slab with a thickness of 20 mm having a pancaked microstructure consisting of austenite within a δ -ferrite (hereafter called ferrite) matrix (Figure 1). Samples with a size of 10 mm \times 10 mm \times 20 mm were cut from the as-received slab. They were reheated at 1370 °C and held 40 min in a muffle furnace in an argon atmosphere to revert austenite back into ferrite. One specimen was immediately water-quenched from 1370 °C. Another specimen was slowly cooled in the furnace from 1370 °C to 970 °C during a 48-h period (i.e. an average cooling rate of \sim 0.002 °C/s). To avoid the formation of precipitates in the temperature range of 900–950 °C [17], the specimen was immediately water-quenched from 970 °C. This heat treatment resulted in the diffusional transformation of ferrite to austenite, forming a microstructure consisting of about 48% austenite with an equiaxed morphology in a ferritic matrix.

A PANalytical X-ray diffractometer was employed to characterise the crystallographic texture of the material. The X-ray diffraction was performed using Cu K α radiation under point focus mode. The texture was measured in the plane containing the rolling direction and normal direction (RD/ND). Due to the presence of coarse grains, a large area of the material was analysed by the aid of a

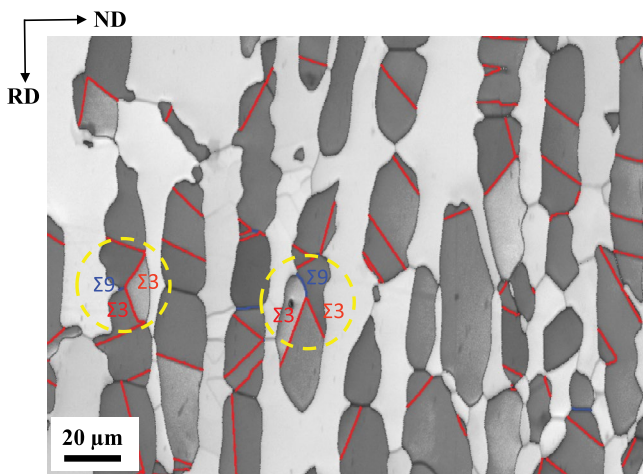


Figure 1. (colour online) EBSD map, in the band contrast colouring, showing the microstructure of the as-received (hot-rolled) duplex stainless steel. The dark grey and light grey areas represent austenite and ferrite, respectively. The red and blue lines are $\Sigma 3$ and $\Sigma 9$ CSL boundaries, respectively. RD and ND represent rolling and normal directions, respectively.

stage oscillation technique with 10 mm of linear movement. This enabled the measurement of an area of about $14 \times 12 \text{ mm}^2$, ensuring the presence of enough grains in the texture analysis. The required inverse pole figures were plotted using the Lambert azimuthal equal-area projection [18].

The specimen for electron backscatter diffraction (EBSD) was prepared on the RD/ND plane, using the standard routine described elsewhere [19]. Multiple EBSD maps were acquired using a FEI FEG Quanta 3-D SEM/FIB under a condition of 20 kV, 8 nA and a working distance of 12 mm. In total, 23 EBSD maps were collected, covering $\sim 63 \text{ mm}^2$ to achieve enough data for the interface plane character analysis using the automated stereological approach. The step size was $1 \mu\text{m}$ with a hexagonal grid. The average confidence index was higher than 0.70 for all the EBSD maps. The acquired maps were then cleaned using TSL-OIM software. First, an iterative grain dilation routine with a 5 pixels grain size minimum was applied to the data. Second, a single average orientation was assigned to each individual grain with a tolerance angle of 5° . The boundaries were then segmented to straight lines using a boundary deviation limit of 2 pixels (i.e. $2 \mu\text{m}$). Due to the presence of two phases, the reconstructed boundaries were classified into three categories, namely (i) ferrite/ferrite, (ii) ferrite/austenite and (iii) austenite/austenite (Table 1). These interfaces were treated separately to analyse the grain boundary plane distribution using the stereological approach [16], described below.

To characterise the grain boundaries (interfaces) in polycrystals, five independent macroscopic parameters are required; three parameters specifying the lattice misorientation and two defining the boundary plane orientation [20]. The former is defined by Euler angles $(\varphi_1, \Phi, \varphi_2)$ or an angle/axis pair $(\theta/[uvw])$, which can be readily measured through the conventional EBSD analysis. Furthermore, each boundary segment is the trace for the grain boundary on the surface plane. Having these measurements, the only remaining parameter to characterise the boundary is the boundary plane inclination with respect to the surface plane. It has recently been shown that if a sufficient number of grain boundary traces for a given angle/axis pair is obtained, the grain boundary plane distribution can be recovered using a stereological approach [21]. Generally, each line segment must be orthogonal to its boundary plane normal. Therefore, all possible plane normals for a particular line segment lie on a great circle, which is perpendicular to that line segment on a stereographic projection. If many grain boundary segments with a fixed lattice misorientation are measured, then a distribution of possible grain boundary normals is defined. In such a case, the most probable planes appear as maxima in the distribution. The planes that are less probable are observed less frequently and

Table 1. Number of segments for different boundaries. δ and γ represent ferrite and austenite phases, respectively.

	δ/δ boundaries		δ/γ boundaries		γ/γ boundaries	
	number	%	number	%	number	%
All interfaces						
92279	2381	2.6	66251	71.8	23647	25.6

assuming they are sampled randomly, this background can be removed [21]. After collecting enough traces (e.g. 50,000 boundary traces for cubic crystal structures [21]), it is possible to measure the preferred orientation of an interface plane. The relative area of different boundaries can then be determined in unit of multiples of a random distribution (i.e. MRD). Relative areas greater than one show that the corresponding plane is more frequently observed in the microstructure than expected in a random distribution. The distributions are discrete and individual boundaries are classified in intervals with an approximately 10° width.

3. Results

3.1. Microstructure and texture evolution

The as-received microstructure consisted of about half austenite and half ferrite, with both phases elongated along the rolling direction (Figure 1). The ferrite showed a relatively strong texture with the (0 0 1) orientation parallel to ND with an intensity of 4.5 times random (Figure 2(a)). The austenite revealed an inverse pole figure characterised by a relatively weak texture with a maximum of ~ 1.7 times random, having a relatively strong (1 0 1) and weak (1 0 0) and (1 1 1) fibres oriented along ND (Figure 2(b)).

The microstructure of the sample subjected to reheating to 1370°C and holding for 40 min followed by rapid water quenching revealed very coarse ferrite grains ($\sim 900\ \mu\text{m}$) along with $\sim 12\%$ fine austenite particles scattered throughout the microstructure (Figure 3). The austenite was observed as both continuous films on the ferrite grain boundaries and dispersed fine lath-shaped particles in the ferrite grain interiors. The characteristics of the lath-like austenite formed in such a microstructure have been thoroughly studied by Ameyama et al. [22,23]. In the presence of both austenite and ferrite, very limited grain growth would be expected during annealing of duplex stainless steel due to the mutual restriction of growth exerted by one phase on the other [24]. In this context, the evidence for significant ferrite grain growth in Figure 3 suggests that the initial austenite was

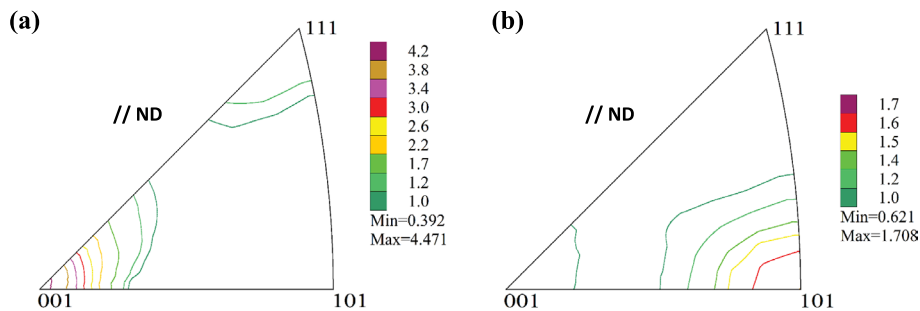


Figure 2. (colour online) Inverse pole figure of the (a) ferrite and (b) austenite phases in the as-received condition.

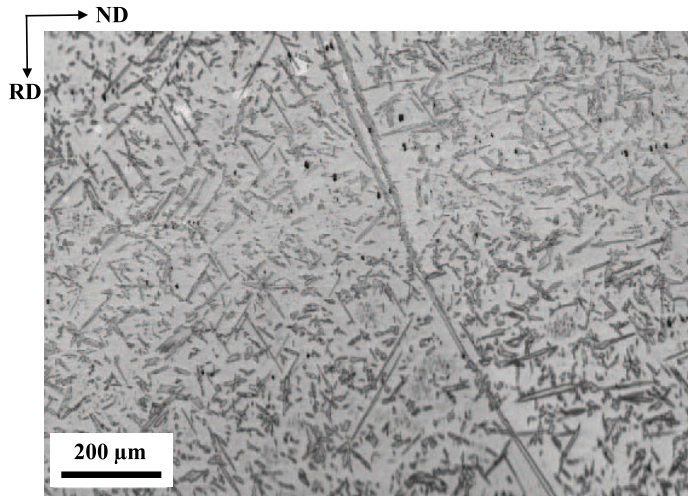


Figure 3. EBSD map, in the band contrast colouring, showing the microstructure of the duplex stainless steel after holding at 1370 °C for 40 min followed by water quenching. The dark grey and light grey areas represent austenite and ferrite, respectively. RD and ND represent rolling and normal directions, respectively.

mostly dissolved during the reheating treatment and the austenite particles were largely formed during water quenching. The formation of austenite at such a high cooling rate is not surprising as the presence of nitrogen promotes the formation of austenite in this grade of duplex steel even at a very fast quenching rate [25].

The sample which was reheated to 1370 °C, held for 40 min and then slowly cooled in the furnace to 970 °C, followed by water quenching, displayed an equiaxed austenite and ferrite microstructure (Figure 4). The austenite grains were observed in both the ferrite grain interiors and on the ferrite–ferrite grain boundaries. No sigma phase was found in the microstructure, suggesting that the sample was quenched well above the ferrite to sigma phase transformation temperature. The equiaxed austenite grains mostly contained $\Sigma 3$ twin boundaries with a $60^\circ/[1\ 1\ 1]$ disorientation along with some $\Sigma 9$ boundaries with a $39^\circ/[1\ 1\ 0]$ disorientation. The $\Sigma 9$ boundaries mostly appeared at the intersection of two $\Sigma 3$ boundaries (as highlighted by the dash circles in Figures 1 and 4).

The ferrite in the heat-treated microstructure qualitatively displayed a similar crystallographic texture to the as-received condition, with the (001) orientation parallel to ND and an intensity of ~ 4.4 times random (Figure 5(a)). Interestingly, the equiaxed austenite also displayed a very similar texture to the as-received condition. The inverse pole figure was characterised by a maximum of ~ 1.9 times random with strong (1 0 1) and (0 0 1) fibres oriented along ND (Figure 5(b)).

There are two possible reasons for the similarity of austenite texture in the transformed and as-received conditions. First, it may imply that the austenite has not been fully dissolved during reheating to 1370 °C, so it has, to some extent, retained its rolling texture, as it re-grows during cooling from 1370 °C. A second possible

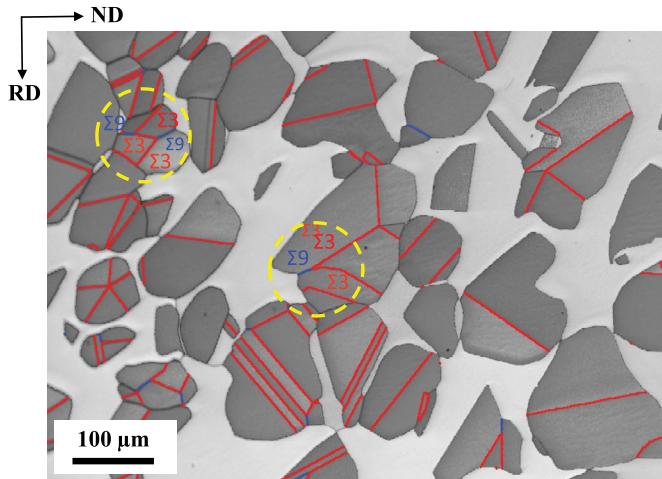


Figure 4. (colour online) EBSD map, in the band contrast colouring, showing the microstructure of the experimental material after the heat treatment at 1370 °C followed by slow cooling to 970 °C. The dark grey and light grey areas represent austenite and ferrite, respectively. The red and blue lines are $\Sigma 3$ and $\Sigma 9$ CLS boundaries, respectively. RD and ND represent rolling and normal directions, respectively.

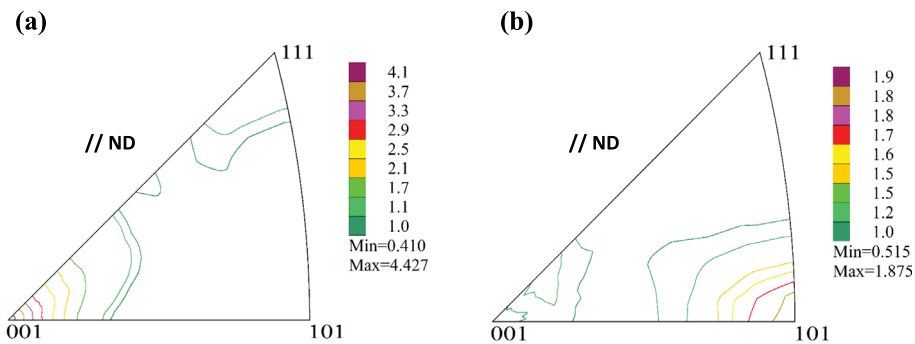


Figure 5. (colour online) Inverse pole figure of the (a) ferrite and (b) austenite phases obtained after heat treatment at 1370 °C followed by slow cooling to 970 °C.

reason for the texture conservation may be the ‘texture memory effect’ [26–28]. It can be expected that an austenite grain transformed into a ferrite grain holds a particular crystallographic orientation relationship during reheating. During the back transformation of the ferrite structure, the same crystallographic austenite variant/s would be preferred to form on cooling, which leads to the same austenite orientation/s resulting in an overall texture similar to the initial one. This is the so-called texture memory phenomenon. A strong texture memory effect has also been observed during the ferrite to austenite and then reverse austenite to ferrite transformation [29]. These observations also strengthen the idea that the transformation texture is dictated by nucleation, i.e. variant selection, and it rarely changes during growth [30].

3.2. Interfaces formed during the ferrite to austenite transformation

The misorientation angle distribution for all of the boundaries in the microstructure showed two main peaks at $\sim 43^\circ$ and 60° (Figure 6(a)). Because there are two phases, the distribution contains ferrite–ferrite, ferrite–austenite and austenite–austenite interfaces. To better understand the phase boundaries, the interfaces were classified by type and their characteristics were studied separately. Most of the boundaries were ferrite–austenite interfaces followed by austenite–austenite and ferrite–ferrite interfaces (Table 1). The ferrite–ferrite interface misorientation angle distribution did not follow any specific trend and was noisy. A number of local maxima had intensities of $\sim 2\%$, but the significance is questionable without additional data (Figure 6(b)). Due to a limited number of ferrite–ferrite segments, no further analysis was carried out on these boundaries.

3.3. Ferrite–austenite interfaces

The misorientation angle distribution of ferrite–austenite interfaces revealed a wide misorientation angle range, spreading from $\sim 10^\circ$ to 62.8° (Figure 6(c)). A single peak appeared at the position of $\sim 43^\circ$. For all misorientations, the distribution of interface planes in austenite had a maximum at the (1 1 1) orientation. The distribution of interface planes in ferrite revealed two local maxima centred at the (1 1 1) and (1 0 1) orientations (Figure 7).

During cooling, the current steel transforms from ferrite (body centred cubic, BCC) to austenite (face centred cubic, FCC). Several orientation relationship models have been proposed between the parent phase and transformed phase in BCC–FCC transformations. These include Bain [31], Kurdjumov–Sachs (K–S) [32], Nishiyama–Wassermann (N–W) [33], Pitsch [34] and Greninger–Troiano (G–T) [35] (Table 2). These ORs are relatively close with a maximum deviation of 5.26° , which exists between the K–S and N–W ORs. Therefore, the ferrite/austenite interfaces were only examined for the K–S and N–W ORs in the present study.

Here, a 2° tolerance angle was used to differentiate the K–S from the N–W OR. Based on that, the ferrite–austenite interfaces were categorised to three groups,

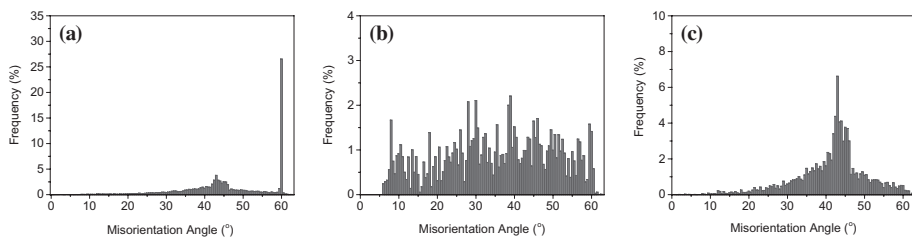


Figure 6. Misorientation angle distribution for (a) all interfaces (including ferrite–ferrite, austenite–ferrite and austenite–austenite), (b) ferrite–ferrite boundaries and (c) ferrite/austenite interfaces after the heat treatment at 1370°C and slow cooling to 970°C .

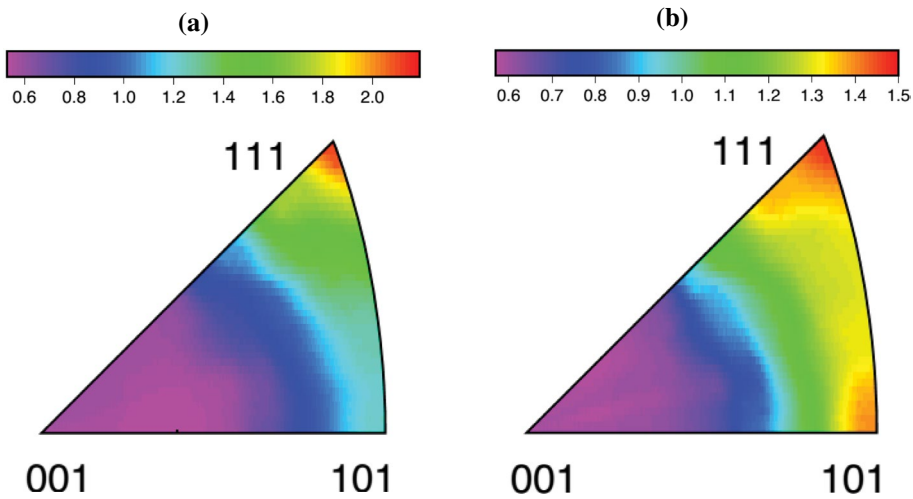


Figure 7. (colour online) Grain boundary plane character distribution at the ferrite–austenite interfaces independent of misorientations: (a) austenite planes and (b) ferrite planes. The colour scale values are in multiples of a random distribution (i.e. MRD).

Table 2. Plane and direction parallelism conditions and misorientation angle–axis pairs between FCC and BCC phases under different orientation relationships. The reference lattice is austenite.

Orientation relationship	Parallelism	Minimum angle-axis pairs	Refs.
Kurdjumov–Sachs (K–S)	$\{1\ 1\ 1\}_{\text{fcc}} // \{1\ 1\ 0\}_{\text{bcc}}$ $\langle 1\ 1\ 0 \rangle_{\text{fcc}} // \langle 1\ 1\ 1 \rangle_{\text{bcc}}$	42.85° $\langle 0.968\ 0.178\ 0.178 \rangle$	[32]
Greninger–Troiano (G–T)	$\{1\ 1\ 1\}_{\text{fcc}} // \{1\ 1\ 0\}_{\text{bcc}}$ $\langle 1\ 2\ 3 \rangle_{\text{fcc}} // \langle 1\ 3\ 3 \rangle_{\text{bcc}}$	44.23° $\langle 0.973\ 0.189\ 0.133 \rangle$	[35]
Bain (B)	$\{1\ 0\ 0\}_{\text{fcc}} // \{1\ 0\ 0\}_{\text{bcc}}$ $\langle 1\ 0\ 0 \rangle_{\text{fcc}} // \langle 1\ 1\ 0 \rangle_{\text{bcc}}$	45° $\langle 1\ 0\ 0 \rangle$	[31]
Pitsch (P)	$\{1\ 0\ 0\}_{\text{fcc}} // \{1\ 1\ 0\}_{\text{bcc}}$ $\langle 1\ 1\ 0 \rangle_{\text{fcc}} // \langle 1\ 1\ 1 \rangle_{\text{bcc}}$	45.98° $\langle 0.08\ 0.2\ 0.98 \rangle$	[34]
Nishiyama–Wassermann (N–W)	$\{1\ 1\ 1\}_{\text{fcc}} // \{1\ 1\ 0\}_{\text{bcc}}$ $\langle 1\ 1\ 2 \rangle_{\text{fcc}} // \langle 1\ 1\ 0 \rangle_{\text{bcc}}$	45.98° $\langle 0.976\ 0.083\ 0.201 \rangle$	[33]

namely K–S, N–W and ‘other’ interfaces. The latter refers to the interfaces which did not fulfil the K–S and N–W ORs criteria (i.e. relevant misorientation angle/axis pairs, Table 2). Considering a 2° tolerance angle, only about 12 and 4% of interfaces were characterised as having the K–S and N–W ORs, respectively. In other words, ~84% of the interfaces were considered as having ‘other’ OR as they did not follow any of the two main orientation relationships (i.e. K–S and N–W) within a 2° tolerance.

The habit plane distributions for both austenite and ferrite were separately calculated for different orientation relationships (i.e. K–S, N–W and other ORs, Figure 8). For austenite, the peak appeared close to (1 1 1) planes for all orientation relationships. However, the peak intensity was not the same for all ORs, showing a maximum of 3.3 MRD for the K–S OR, 2.5 for N–W OR and 2.1 for other ORs. Moreover, the relative areas of (110) austenite planes was moderate (i.e. ~1.3 MRD), while (0 0 1) austenite planes were rarely observed (i.e. ~0.6 MRD).

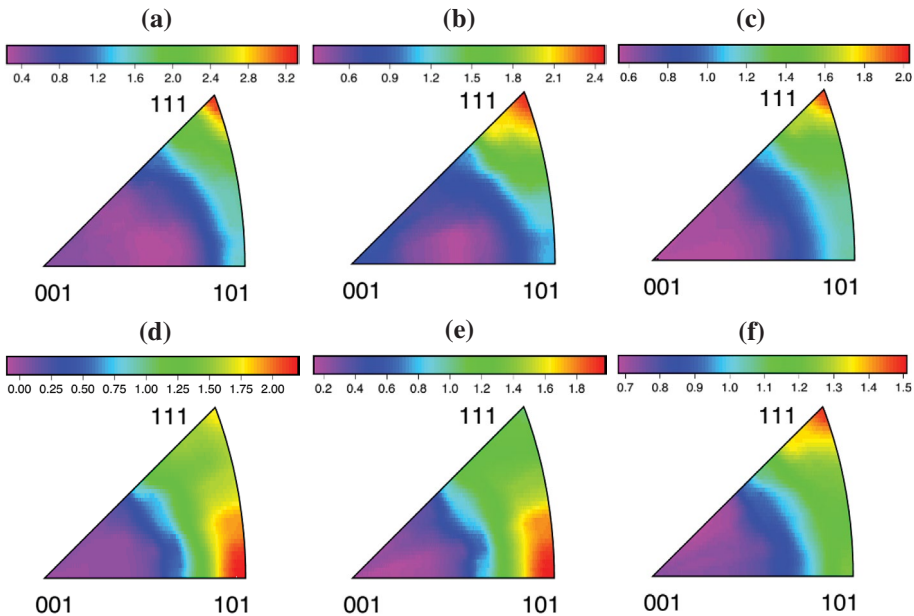


Figure 8. (colour online) The two-parameter grain boundary plane distribution calculated from line segments with a specific orientation relationship and combination of phases. (a) austenite (K–S), (b) austenite (N–W), (c) austenite (other), (d) ferrite (K–S), (e) ferrite (N–W), (f) ferrite (other). The colour scale values are in MRD.

By contrast, ferrite showed distinct habit plane character distributions for different orientation relationships. The ferrite habit plane distributions associated with the K–S and N–W ORs were qualitatively similar, having a peak at the (1 0 1) orientation, spreading towards (1 1 1) planes. The peak at (1 0 1) ferrite was greater for the K–S OR (~ 2.2 MRD) compared with the N–W OR (~ 2.0 MRD). The other interfaces displayed a significantly different distribution, showing a maximum at the (1 1 1) orientation (~ 1.5 MRD), spreading towards the (1 0 1) orientation (~ 1.2 MRD). For all ORs, the ferrite habit planes were rarely terminated by the (0 0 1) orientation.

3.4. Austenite–austenite interfaces

The misorientation angle distribution for the austenite–austenite interfaces displayed a strong peak at 60° and a small peak in the range of $38\text{--}40^\circ$ (Figure 9). The misorientation axis distribution associated with these peaks revealed a maxima at the position of [1 0 1] and [1 1 1] for the misorientation angles of 39° and 60° , respectively (Figure 10). These misorientation angle/axis characteristics represent the $\Sigma 3$ (i.e. $60^\circ/[1\ 1\ 1]$) and $\Sigma 9$ (i.e. $38.9^\circ/[1\ 1\ 0]$) boundaries, which are consistent with the observations in Figure 4. The corresponding plane distributions for $\Sigma 3$ and $\Sigma 9$ boundaries were measured using the stereological approach. For $\Sigma 3$ boundaries, there was a single sharp peak centred at the orientation of the

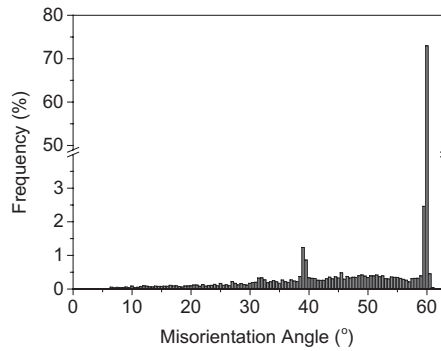


Figure 9. Misorientation angle distribution for the austenite/austenite boundaries. The colour scale values are in MRD.

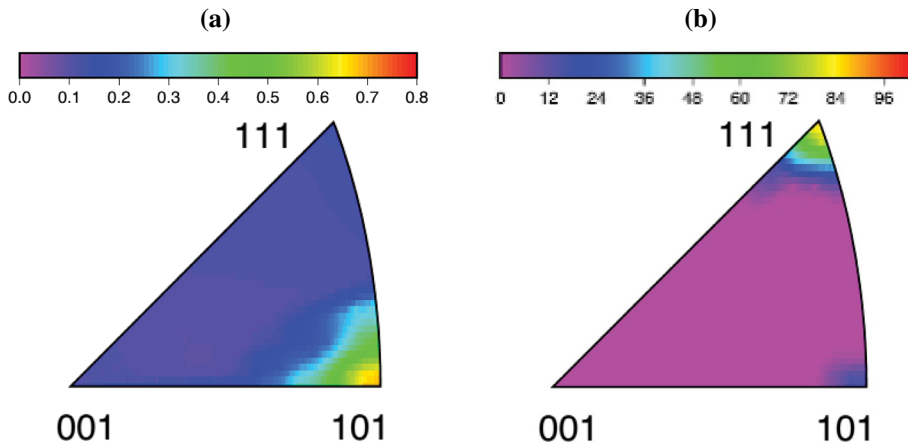


Figure 10. (colour online) Misorientation axis distribution for the $\Sigma 3$ and $\Sigma 9$ austenite/austenite CSL boundaries. The colour scale values are in MRD.

(1 1 1) twist boundary, showing a significant population of ~ 3200 MRD (Figure 11(a)). For $\Sigma 9$, the most common boundaries were located on the zone of tilt boundary positions. There were local maxima centred on the $(\bar{1}13)$, $(3\bar{3}2)$ and $(1\bar{1}4)$ tilt boundary orientations with a value of ~ 5.5 MRD (Figure 11(b)). Moreover, a relatively weak intensity was also observed at the $(\bar{2}21) \parallel (\bar{2}21)$ symmetric tilt boundary position. The plane distribution for all of the austenite–austenite boundaries, irrespective of misorientation, showed a sharp peak at the (1 1 1) orientation, with an intensity of ~ 6.8 MRD (Figure 11(c)).

There were also some boundaries with misorientation angles other than 39° and 60° (Figure 9). These boundaries may have been formed once two distinctly orientated growing austenite grains intersected. For simplicity, it is assumed that these austenite grains were formed through the K–S OR from the parent ferrite during the phase transformation on cooling. Therefore, 24 equivalent crystallographic K–S-orientated austenite grains (i.e. variants) can be theoretically formed

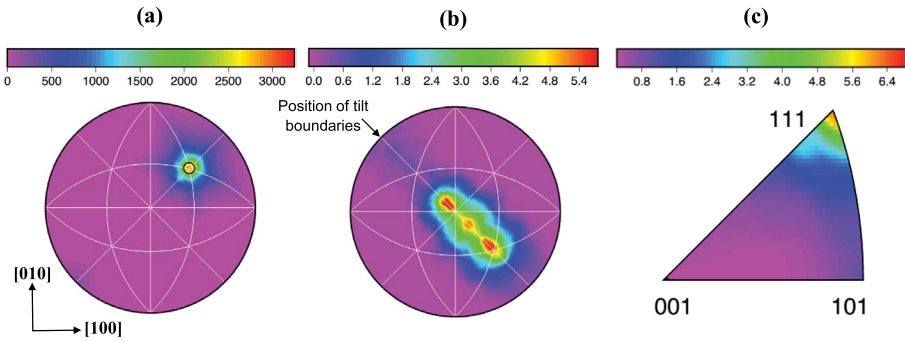


Figure 11. (colour online) Grain boundary character distribution at a fixed misorientation of (a) $60^\circ/[1\ 1\ 1]$, and (b) $38.9^\circ/[1\ 1\ 0]$ plotted in the $[0\ 0\ 1]$ stereographic projection. The circle in (a) represents the position of pure twist boundary. (c) The grain boundary character distribution for the austenite–austenite boundaries irrespective of misorientations. The colour scale values are in MRD.

based on the symmetry of the cubic system from a particular ferrite parent grain. The misorientation angle/axis pairs associated with the intersection of two distinct grain orientations/variants are given in Table 3, taking austenite as the reference lattice. Due to the crystal symmetry, the number of angle/axis pairs can be reduced from 23 to 16 [36].

The grain boundary plane distribution of austenite was plotted for all misorientations related to the K–S OR (i.e. K–S inter-variant boundaries, Figures 11(a), 12,

Table 3. Possible 24 variants generated through phase transformation having the K–S orientation relationship. δ and γ represent ferrite and austenite phases, respectively. The reference lattice is austenite.

Variant	Plane parallel	Direction parallel	Rotation angle/axis from V1
V1	$(1\ 1\ 1)_\gamma \parallel (0\ 1\ 1)_\delta$	$[\bar{1}\ 0\ 1]_\gamma \parallel [\bar{1}\ \bar{1}\ 1]_\delta$	–
V2		$[\bar{1}\ 0\ 1]_\gamma \parallel [\bar{1}\ 1\ \bar{1}]_\delta$	$60^\circ/[1\ 1\ \bar{1}]$
V3		$[0\ 1\ \bar{1}]_\gamma \parallel [\bar{1}\ \bar{1}\ 1]_\delta$	$60^\circ/[0\ 1\ 1]$
V4		$[0\ 1\ \bar{1}]_\gamma \parallel [\bar{1}\ 1\ \bar{1}]_\delta$	$10.5^\circ/[0\ \bar{1}\ \bar{1}]$
V5		$[1\ \bar{1}\ 0]_\gamma \parallel [\bar{1}\ \bar{1}\ 1]_\delta$	$60^\circ/[0\ \bar{1}\ \bar{1}]$
V6		$[1\ \bar{1}\ 0]_\gamma \parallel [\bar{1}\ 1\ \bar{1}]_\delta$	$49.5^\circ/[0\ 1\ 1]$
V7	$(1\ \bar{1}\ 1)_\gamma \parallel (0\ 1\ 1)_\delta$	$[1\ 0\ \bar{1}]_\gamma \parallel [\bar{1}\ \bar{1}\ 1]_\delta$	$49.5^\circ/[\bar{1}\ \bar{1}\ 1]$
V8		$[1\ 0\ \bar{1}]_\gamma \parallel [\bar{1}\ 1\ \bar{1}]_\delta$	$10.5^\circ/[1\ 1\ \bar{1}]$
V9		$[\bar{1}\ \bar{1}\ 0]_\gamma \parallel [\bar{1}\ \bar{1}\ 1]_\delta$	$50.5^\circ/[\bar{1}\ 0\ 3\ \bar{1}\ \bar{3}]$
V10		$[\bar{1}\ \bar{1}\ 0]_\gamma \parallel [\bar{1}\ 1\ \bar{1}]_\delta$	$50.5^\circ/[\bar{7}\ 5\ 5]$
V11		$[0\ 1\ 1]_\gamma \parallel [\bar{1}\ 1\ 1]_\delta$	$14.9^\circ/[1\ 3\ 5\ 1]$
V12		$[0\ 1\ 1]_\gamma \parallel [\bar{1}\ 1\ \bar{1}]_\delta$	$57.2^\circ/[\bar{3}\ 5\ 6]$
V13	$(\bar{1}\ 1\ 1)_\gamma \parallel (0\ 1\ 1)_\delta$	$[0\ \bar{1}\ 1]_\gamma \parallel [\bar{1}\ \bar{1}\ 1]_\delta$	$14.9^\circ/[5\ \bar{1}\ 3\ 1]$
V14		$[0\ \bar{1}\ 1]_\gamma \parallel [\bar{1}\ 1\ \bar{1}]_\delta$	$50.5^\circ/[\bar{5}\ 5\ \bar{7}]$
V15		$[\bar{1}\ 0\ \bar{1}]_\gamma \parallel [\bar{1}\ \bar{1}\ 1]_\delta$	$57.2^\circ/[\bar{6}\ 2\ 5]$
V16		$[\bar{1}\ 0\ \bar{1}]_\gamma \parallel [\bar{1}\ 1\ \bar{1}]_\delta$	$20.6^\circ/[\bar{1}\ 1\ \bar{1}\ \bar{6}]$
V17		$[1\ 1\ 0]_\gamma \parallel [\bar{1}\ \bar{1}\ 1]_\delta$	$51.7^\circ/[\bar{1}\ \bar{1}\ 6\ \bar{1}\ \bar{1}]$
V18		$[1\ 1\ 0]_\gamma \parallel [\bar{1}\ 1\ \bar{1}]_\delta$	$47.1^\circ/[\bar{2}\ 4\ \bar{1}\ 0\ 2\ 1]$
V19	$(1\ 1\ \bar{1})_\gamma \parallel (0\ 1\ 1)_\delta$	$[\bar{1}\ 1\ 0]_\gamma \parallel [\bar{1}\ \bar{1}\ 1]_\delta$	$50.5^\circ/[\bar{3}\ 1\ 3\ 1\ 0]$
V20		$[\bar{1}\ 1\ 0]_\gamma \parallel [\bar{1}\ 1\ \bar{1}]_\delta$	$57.2^\circ/[3\ 6\ \bar{5}]$
V21		$[0\ \bar{1}\ \bar{1}]_\gamma \parallel [\bar{1}\ \bar{1}\ 1]_\delta$	$20.6^\circ/[3\ 0\ \bar{1}]$
V22		$[0\ \bar{1}\ \bar{1}]_\gamma \parallel [\bar{1}\ 1\ \bar{1}]_\delta$	$47.1^\circ/[\bar{1}\ 0\ 2\ 1\ 2\ 4]$
V23		$[1\ 0\ 1]_\gamma \parallel [\bar{1}\ \bar{1}\ 1]_\delta$	$57.2^\circ/[\bar{2}\ 5\ \bar{6}]$
V24		$[1\ 0\ 1]_\gamma \parallel [\bar{1}\ 1\ \bar{1}]_\delta$	$21.1^\circ/[9\ 4\ 0]$

and 13). For the misorientation axis of $\langle 1\ 1\ 1 \rangle$, the distribution of planes depended on the misorientation angle (Figures 11(a) and 12). At a misorientation of 10.53° (Figure 12(a)), there were multiple peaks with low intensities at positions of $\{1\ 1\ 1\}$ and $\{1\ 1\ 0\}$ planes. The most intense peak appeared at the position of the $(1\ 1\ 1)$ twist boundary plane. The diffuse peaks at positions of $\{1\ 1\ 0\}$ correspond to symmetric tilt boundaries (Figure 12(a)). At the misorientation of 49.47° , a single sharp peak was observed at the $(1\ 1\ 1)$ orientation with 5 MRD, which is a twist boundary (Figure 12(b)). At 60° , the distribution is the same, though the intensity significantly increased to ~ 3200 MRD, representing $\Sigma 3$ boundaries (Figure 11(a)).

It should be emphasised here that the very high concentration of $\Sigma 3$ boundaries in the austenite, together with the way the data are discretely binned, can distort the distribution at nearby disorientations. For example, the distribution of grain boundary planes for disorientations at $49.5^\circ/[1\ 1\ 1]$ and $60^\circ/[1\ 1\ 0]$ is 10.5° from the $\Sigma 3$ disorientation that has equivalent representations at $60^\circ/[1\ 1\ 1]$ and $70.5^\circ/[1\ 1\ 0]$. In these cases, all grain boundary traces within Brandon's criterion of $\Sigma 3$ were first removed from the data-set before computing the distribution.

For the misorientation axis of $\langle 1\ 1\ 0 \rangle$, the grain boundary plane distribution varies significantly with the misorientation angle (Figure 13). At the misorientation of 10.53° , the planes were distributed mostly at $\{1\ 1\ 1\}$ and $\{1\ 1\ 0\}$ positions, having a very weak intensity of 0.7 MRD (Figure 13(a)). The distribution of planes at the misorientation of 49.47° revealed a peak at the $(\bar{3}\ \bar{1}\ 3)$ orientation with an intensity of 2.3 MRD, extending toward the $(\bar{1}\ 0\ 0)$ and $(\bar{1}\ \bar{1}\ 1)$ orientations. At the misorientation angle of 60° , the distribution showed multiple peaks with an intensity of ~ 2.4 MRD at the $(1\ 1\ 0)$ and $(1\ 1\ 1)$ orientations. The distribution of grain boundary planes for all of the other inter-variant boundaries with high

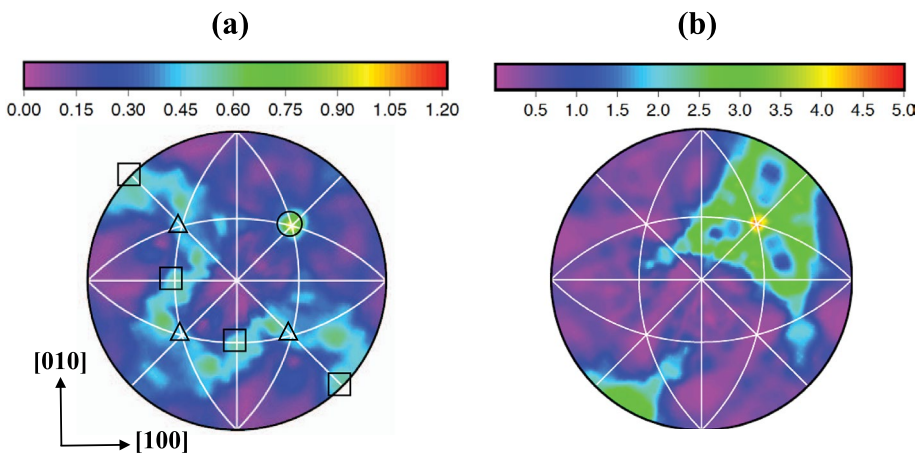


Figure 12 (colour online) Distribution of boundary planes character for austenite–austenite boundaries with different misorientations around $[1\ 1\ 1]$ axis: (a) $10.53^\circ/[1\ 1\ 1]$, (b) $49.47^\circ/[1\ 1\ 1]$. The squares represent the positions of $\{1\ 1\ 0\}$ symmetric tilt boundaries. The circle and triangle mark the location for $\{1\ 1\ 1\}$ twist and mixed boundaries, respectively. The colour scale values are in MRD.

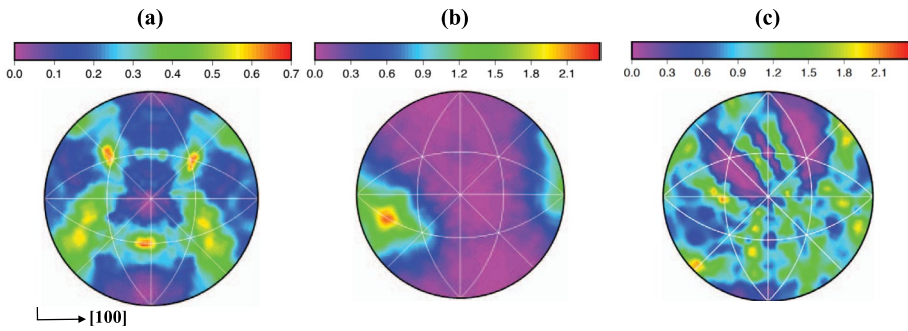


Figure 13. (colour online) Distribution of boundary planes character for austenite–austenite boundaries with different misorientations around $[0\ 1\ 1]$ axis: (a) $10.53^\circ/[0\ 1\ 1]$, (b) $49.47^\circ/[0\ 1\ 1]$, (c) $60^\circ/[0\ 1\ 1]$. The colour scale values are in MRD.

index axes corresponding to the K–S OR was examined. However, the maxima did not exceed 0.8 MRD and were, therefore, considered insignificant.

4. Discussion

4.1. Ferrite–austenite interfaces

Among different interfaces in the heat-treated duplex stainless steel, the highest interface fraction/population belongs to the ferrite–austenite interfaces (i.e. $\sim 71.8\%$), which are mostly formed through the ferrite to austenite transformation on cooling from 1370°C . The distribution of misorientation angles across the ferrite–austenite interfaces shows a wide range between 10 and 62.8° with a considerable amount of interfaces having misorientations lying between 42 and 46° (Figure 6(c)). According to the theoretical ORs [31–35], the misorientation angle distribution of ferrite–austenite interfaces theoretically lies between 42 and 46° (Table 2). There are two possible reasons that some misorientations are not within this ideal range. One has to do with the characteristics of the austenite nuclei that form at the parent ferrite–ferrite boundaries at relatively high temperatures. The austenite nuclei interface can be classified into three types, having: (i) K–S/N–W interfaces with both ferrite grains at either side of the boundary; (ii) a K–S/N–W interface with only one grain and (iii) non-KS/NW interfaces with both ferrite grains. The former is less likely to take place in the current study as it requires very high undercooling (e.g. martensitic transformation) and has been rarely reported during the diffusional transformation [37–39]. In the current study, the ferrite–austenite phase transformation occurs in a relatively high temperature range (i.e. during slow cooling from $\sim 1370^\circ\text{C}$). At these high temperatures, the difference in the barrier for the nucleation of austenite with a K–S/N–W or other orientation interface is not as large as at low temperature, and both processes are competitive. As long as both processes occur, not all ferrite–austenite interfaces will fully fulfil K–S/N–W orientation relationship requirements.

A second reason that misorientations are found outside of the ideal range is suggested by the presence of a similar austenite overall texture in the as-received and heat-treated conditions (Figures 2 and 5). One possible reason for the similarity of the texture is that the initial microstructure may not fully be transformed to ferrite at 1370 °C and some residual austenite would still remain at such a high temperature. The microstructure of the as-received material reveals that it was subjected to a hot rolling process (Figure 1). Therefore, the ferrite–austenite interfaces in the as-received condition are expected to significantly deviate from the original K–S/N–W OR characteristics due to the hot deformation. In other words, the residual austenite most likely has the other OR with the adjacent ferrite, which would be preserved during further growth on cooling. As a result, the overall misorientation angle distribution of austenite and ferrite is spread beyond the range one expects for the ideal ORs (Figure 6(c)).

For the misorientation angle range of 40–50°, the interphase plane distribution of austenite reveals a strong anisotropy, exhibiting a peak at the (1 1 1) orientation with an intensity of ~ 2.2 MRD (Figure 7(a)). This is consistent with the crystallographic preference associated with the K–S and N–W ORs and low energy configuration of closed packed planes in the FCC structure, as reported for single-phase FCC materials [40–42]. However, the interphase plane distributions of ferrite display two main peaks at the positions of (1 1 0) and (1 1 1) planes (Figure 7(b)). The former is consistent with the crystallographic preference associated with rational ORs and because it is the close packed plane in the BCC structure (i.e. it is a low energy interface) [43]. A high relative area of (1 1 1) planes was recently reported in a single phase ferritic structure, and this was attributed to the presence of a strong gamma fibre ($\langle 1\ 1\ 1 \rangle // \text{ND}$) texture [44]. However, this cannot be linked to the ferrite texture in the current study, where the ferrite displays a strong (0 0 1) fibre texture (see Figure 5(a)). In addition, the ferrite–austenite interfaces form by a phase transformation rather than other processes, such as grain growth and recrystallisation, that create grain boundaries in single-phase materials. To explore further, the ferrite–austenite interfaces can be classified into three categories based on the main rational ORs, namely K–S, N–W and other ORs.

A further analysis of the ferrite–austenite interfaces reveals that 12 and 4% of the ferrite–austenite interfaces were consistent with the K–S and N–W ORs (with a 2° tolerance angle), respectively. For both the K–S and N–W ORs, austenite and ferrite grains terminate on (1 1 1) and (1 1 0) planes, respectively (Figure 8(a,b,d,e)). This is not surprising as these planes are the crystallographically favoured parallel planes (i.e. close packed planes) in the theoretical ORs during the BCC to FCC transformation. In the equilibrium condition, these interfaces are flat at an atomic level and mostly free of steps having misfit dislocations characterised by in-plane Burgers vectors [45]. Even for a non-flat interface, it has been suggested that the degree of coherency could be enhanced and the energy would be minimised by creating a stepped $(1\ 1\ 1)_{\text{FCC}} // (1\ 1\ 0)_{\text{BCC}}$ configuration [46].

The predominance of $(1\ 1\ 1)_{\text{FCC}}// (1\ 1\ 0)_{\text{BCC}}$ interfaces is also in line with the minimum energy plane considerations. Using the first nearest neighbour broken bond model, the relative surface free energies of FCC and BCC phases on either side of interphase were determined to have minima at the $(1\ 1\ 1)$ and $(1\ 1\ 0)$ plane orientations, respectively [47]. The relative areas of these planes are inversely correlated to the surface energies, as these orientations correspond to maxima in the austenite and ferrite interface plane distributions for those interfaces that meet the K–S and N–W ORs criteria (Figure 8(a,b,d,e)). These planes are also close to, though not exactly the same as, the estimates made based on Near-Coincidence Site geometrical matching of BCC-FCC lattices [48–50]. Note that interfaces consisting of $(1\ 1\ 1)_{\text{FCC}}// (1\ 1\ 0)_{\text{BCC}}$ planes have been recently reported in a nanobainitic steel formed through shear transformation at a relatively low temperature [16].

For the interfaces which do not correspond to the K–S and N–W orientation relationships, both ferrite and austenite tend to terminate on $(1\ 1\ 1)$ planes (Figure 8(c) and (f)). The difference in ferrite planes for K–S/N–W and other ferrite–austenite interfaces may stem from the nucleation behaviour of austenite at an early stage of transformation. The two most important factors controlling the phase transformation are interfacial and strain energies accompanying the transformation [51]. A shear transformation is accompanied by a shape deformation, which plays the most important role in the nucleation behaviour. In the diffusional transformation, however, there is a limited shape deformation, which is expected to be relaxed in a relatively high transformation temperature regime (e.g. upon slowly cooling from 1370 °C). In such a case, the interfacial energy is more influential in the nucleation process than the strain energy. During the austenite to ferrite transformation, it was demonstrated that the OR between ferrite nuclei and parent austenite strongly depends on the austenite–austenite grain boundary character (i.e. low energy boundaries promote the rational ORs) [38]. Therefore, it would be expected that ferrite boundaries terminated by $(1\ 1\ 0)$ planes trigger the formation of austenite nuclei with the favoured crystallography and low energy interfaces (i.e. K–S and N–W ORs), at least with one of the parent ferrite grains during the ferrite to austenite transformation. In other words, the nucleation of austenite on ferrite/ferrite boundaries with non- $(1\ 1\ 0)$ planes may promote the other ORs. Finally, it is to be noted that the predominance of $(1\ 1\ 1)$ ferrite planes for non-KS/NW interfaces formed during phase transformation contrasts with the findings of Watanabe [52] for irrational interfaces formed by recrystallisation in a single-phase ferritic steel. During the diffusional recrystallisation of a Fe-3%Si alloy, a $\{1\ 1\ 0\}$ plane-matching OR was found to be the more widespread as it ensures high boundary mobility during grain growth [52].

Another interesting aspect of the current results is the preference of the K–S orientation relationship over N–W in duplex stainless steels, which is also evident in their interface plane distributions (Figure 8(a,b,d,e)). It is generally known that twinned austenite grains show a 180° rotation around the $\langle 1\ 1\ 2 \rangle$ direction (equivalent to 60°/ $\langle 1\ 1\ 1 \rangle$). One rotation angle-axis representation associated with the

K–S OR is $90^\circ/\langle 1\ 1\ 2 \rangle$, as proposed by Jonas et al. [53]. This shows that multiple twinning of a K–S related austenite would conserve its OR with respect to the parent ferrite grain. However, such a conservation of OR would not work for the N–W as perfectly as it does for the K–S since the angle/axis for N–W is $90.12^\circ/\langle -0.348, 0.841, 0.413 \rangle$. This has a deviation from $90^\circ/\langle -1\ 2\ 1 \rangle$ [53]. Moreover, it has been reported that the atomic mismatch in the case of the K–S OR is less than for the N–W OR [54]. This, together with the fact that the invariant line lies close to the common close-packed directions for the K–S (i.e. $\langle 1\ 1\ 1 \rangle_{\text{F}}//\langle 0\ 1\ 1 \rangle_{\text{A}}$), which is different from the ones associated with the N–W OR (i.e. $\langle 1\ 0\ 0 \rangle_{\text{F}}//\langle 0\ 1\ 1 \rangle_{\text{A}}$) in the BCC–FCC interfaces [55], may be another possible reason for the predominance of the K–S OR. El Hajjaji [56] studied the prevalence of the K–S and N–W ORs in different duplex stainless steels and found that the N–W OR is more frequently observed in high-purity duplex stainless steels. The addition of carbon and/or sulphur, however, locally changed the structure of the interface towards the K–S OR.

4.2. Austenite–austenite interfaces

The misorientation angle distribution for austenite–austenite boundaries shows a sharp peak at 60° (Figure 9). The corresponding axes reveal that $\Sigma 3$ (i.e. $60^\circ/[1\ 1\ 1]$) boundaries comprised the highest population of austenite–austenite boundaries (Figures 9 and 10). This is typical for FCC materials with low SFEs that are known to develop a high fraction of twins. An analysis of the boundaries shows that the number (length) fraction of $\Sigma 3$ austenite–austenite boundaries is 49% (77%). This is comparable to previous studies reporting that 63% (58%) of boundaries in nickel (copper) have the $\Sigma 3$ disorientation [42]. This difference may be attributed to different factors such as the chemical composition, which dictates the SFE value, overall texture, grain size and thermomechanical processing history. The second significant peak in the misorientation angle distribution is at 38.9° and is associated with a $[1\ 1\ 0]$ misorientation axis (i.e. $\Sigma 9$). It is well known that the $\Sigma 9$ misorientation is a geometric consequence of two intersecting $\Sigma 3$ s [40]. In this context, one would expect a relatively high population of $\Sigma 9$ s due to the high fraction of $\Sigma 3$ s. This is not, however, the case in the present duplex stainless steel because very few $\Sigma 3$ s meet at the triple junctions, and most of them terminate at ferrite–austenite interfaces (Figure 4).

The boundaries with the $\Sigma 3$ misorientation within Brandon's criterion [57] were compared with the coherent twin orientation. $\Sigma 3$ boundaries with grain boundary plane orientations within $\pm 10^\circ$ of the ideal twin orientation were classified as coherent, while the rest were classified as incoherent. These boundaries are expected to invert the regular A–B–C stacking sequence of close packed $\{1\ 1\ 1\}$ layers at the boundary plane. Because the nearest and the next-nearest-neighbour atom positions are unchanged, these grain boundaries have the minimum energy [58]. This study finds that the number (length) fraction of all austenite–austenite

coherent $\Sigma 3$ boundaries is 42% (71%). This is mostly higher than the corresponding values specified in previous reports for TWIP steel (9.7% number fraction and 14.6% length fraction) [40], high-purity Ni (28.6% length fraction) [59] and grain boundary engineered brass ($\sim 57\%$ number fraction and $\sim 38\%$ length fraction) [60]. It has been documented that the properties of $\Sigma 3$ grain boundaries depend upon whether they are coherent or incoherent. In this context, the abundance of coherent $\Sigma 3$ s in austenite in this duplex stainless steel compared to other low SFE metals is a very interesting observation. This may be because twins are formed in the present steel at high temperature, during the slow cooling from ~ 1370 °C.

The grain boundary plane distribution is consistent with the finding that 71% of the $\Sigma 3$ boundary area is made up of coherent twins; this results in a maximum at the $(1\ 1\ 1)$ orientation (Figure 11(a)). In this representation, these coherent twin boundaries have twist character, as the grain boundary normal is parallel to the misorientation axis. As noted above, large relative areas of $(1\ 1\ 1)$ planes for $\Sigma 3$ boundaries has been also shown for different FCC materials [39–41,58], and it is also known to be a boundary configuration with minimum energy [38]. Grain boundary plane distributions for $\Sigma 9$ boundaries exhibit maxima along the zone of tilt boundaries (Figure 11(b)) due to the geometrical constraints linked to the intersection of two $\Sigma 3$ boundaries [40]. This is also in a good agreement with the previous reports revealing a maximum population for $\Sigma 9$ boundaries with tilt character, where the misorientation axis is perpendicular to the grain boundary plane normal. It was demonstrated that these plane positions have the minimum energy at this misorientation [40].

The intervariant boundary plane distributions exhibit $\{1\ 1\ 1\}$ normals more frequently than other planes in most of the misorientation angle/axis pairs associated with the K–S OR. In general, the intervariant boundaries with the misorientation axes of $[1\ 1\ 0]$ and $[1\ 1\ 1]$ exhibit higher relative areas compared to the boundaries with higher index axes associated with K–S OR (Figures 10(a), 12, and 13). It is interesting to note that for the misorientation axis of $\langle 1\ 1\ 1 \rangle$, the inter-variant planes for austenite mainly have twist character centred at $\{1\ 1\ 1\}$ orientations (Figures 11(a) and 12). This is different from the result obtained for the product of FCC to BCC transformations (e.g. martensite [61] and bainite [62]), where the most common boundaries have $\{1\ 1\ 0\}$ symmetric tilt orientations.

The current results on austenite–austenite boundaries show that $\Sigma 3$ and inter-variant boundaries tend to terminate on $\{1\ 1\ 1\}$ while $\Sigma 9$ boundaries terminate on planes perpendicular to $[1\ 1\ 0]$ (they have tilt character). However, the formation of these boundaries is associated with different mechanisms/constraints. $\Sigma 3$ twin boundaries were largely formed during the growth of austenite nuclei [63]. This is evident from the presence of $\Sigma 3$ boundaries in most austenite grains (Figure 4). It should be noted that the $\Sigma 3$ disorientation may also form as a result of the impingement of two K–S variants (Table 3); however, the expected frequency is low [36]. The termination of $\Sigma 3$ boundaries on $\{1\ 1\ 1\}$ twist planes is

predominantly associated with the minimum energy boundary plane configuration (Figure 11(a)) [40]. In the case of $\Sigma 9$ boundaries, the geometrical constraints linked to the intersection of two $\Sigma 3$ boundaries dictate the tilt character of grain boundary plane (Figure 11(b)) [40]. The austenite–austenite intervariant boundaries are formed through the ferrite to austenite transformation. Therefore, it would be expected that their boundary planes are governed by the crystallographic preference associated with the ferrite to austenite transformation. Considering a K–S crystallographic OR (i.e. $\{1\ 1\ 0\}\langle 1\ 1\ 1\rangle_{\text{F}}//\{1\ 1\ 1\}\langle 0\ 1\ 1\rangle_{\text{A}}$) during the phase transformation, two growing austenite variants will, most likely, impinge on $\{1\ 1\ 1\}$ planes. This is in good agreement with the current results demonstrating a considerable fraction of inter-variant boundaries terminated at $\{1\ 1\ 1\}$ planes (Figures 10(a), 12 and 13).

5. Conclusions

In the current study, the crystallographic texture and characteristics of interfaces were studied for a duplex stainless steel, produced through the ferrite to austenite phase transformation occurring during slow furnace cooling from 1370 °C. The main findings are:

- (1) Only about 12 and 4% of ferrite–austenite interfaces displayed the K–S and N–W ORs, respectively. The high population of other interfaces was attributed to the nucleation of austenite at high temperatures and/or remnants of some undissolved austenite grains during reheating to 1370 °C.
- (2) Ferrite–austenite interfaces with K–S or N–W ORs were largely terminated on $(1\ 1\ 1)_{\text{FCC}}$ and $(1\ 1\ 0)_{\text{BCC}}$ planes, respectively, which was mostly attributed to the crystallographic preference associated with the phase transformation.
- (3) For ferrite–austenite interfaces with other ORs, both austenite and ferrite habit planes had $(1\ 1\ 1)$ orientations.
- (4) $\Sigma 3$ twin boundaries comprised the majority of austenite–austenite interfaces and mostly showed a twist character, terminating on $(1\ 1\ 1)$ planes because this is the minimum energy configuration. The second highest populated austenite–austenite boundary misorientation was $\Sigma 9$, which tended to terminate on tilt grain boundary planes perpendicular to $[1\ 1\ 0]$. This is a low energy configuration, but geometric constraints might also play a role.
- (5) The intervariant crystallographic plane distribution associated with the K–S OR displayed a general tendency for the austenite habit planes to terminate on the $(1\ 1\ 1)$ orientation, mainly because of the crystallographic preference associated with the phase transformation.

Acknowledgements

The present work was carried out with the support of the Deakin Advanced Characterisation Facility. Financial support provided by the Australian Research Council is gratefully acknowledged.

Disclosure statement

No potential conflict of interest was reported by the authors.

Funding

This work was supported by the Australian Research Council.

References

- [1] R.N. Gunn, *Duplex Stainless Steels: Microstructure, Properties and Applications*, Woodhead Publishing, Cambridge, 1997.
- [2] N. Haghdad, D. Abou-Ras, P. Cizek, P.D. Hodgson, A.D. Rollett, and H. Beladi, *Austenite-ferrite interface crystallography dependence of sigma phase precipitation using the five-parameter characterization approach*, *Mater. Let.* 196 (2017), pp. 264–268.
- [3] N. Haghdad, P. Cizek, H. Beladi, and P.D. Hodgson, *Dynamic restoration processes in a 23Cr–6Ni–3Mo duplex stainless steel: Effect of austenite morphology and interface characteristics*, *Metal. Mater. Trans.* 48 (2017), pp. 4803–4820.
- [4] A. Iza-Mendia, *Altzairu herdoilgaitz duplex austenoferritiko berotako konformazioaren optimizazio: Mikroegitura-karakterizazioa*, Doctoral thesis, University Of Navarra, San Sebastian, 1999.
- [5] T. Watanabe, *Grain boundary engineering: historical perspective and future prospects*, *J. Mater. Sci.* 46 (2011), pp. 4095–4115.
- [6] M.C. Marinelli, A. El Bartali, J.W. Signorelli, P. Evrard, V. Aubin, I. Alvarez-Armas, and S. Degallaix-Moreuil, *Activated slip systems and microcrack path in LCF of a duplex stainless steel*, *Mater. Mater. Sci. Eng. A* 509 (2009), pp. 81–88.
- [7] B. Verhaeghe, F. Louchet, B. Doisneau-Cottignies, Y. Bréchet, and J.P. Massoud, *Micromechanisms of deformation of an austenoferritic duplex stainless steel*, *Phil. Mag. A* 76 (1997), pp. 1079–1091.
- [8] A. Piñol-Juez, A. Iza-Mendia, and I. Gutiérrez, *δ/γ interface boundary sliding as a mechanism for strain accommodation during hot deformation in a duplex stainless steel*, *Metall. Mater. Trans. A* 31 (2000), pp. 1671–1677.
- [9] A. Iza-Mendia, A. Piñol-Juez, J.J. Urcola, and I. Gutiérrez, *Microstructural and mechanical behaviour of a duplex stainless steel under hot working conditions*, *Metall. Mater. Trans. A* 29 (1998), pp. 2975–2986.
- [10] Y.S. Sato and H. Kokawa, *Preferential precipitation site of sigma phase in duplex stainless steel weld metal*, *Scr. Mater.* 40 (1999), pp. 659–663.
- [11] D. Qiu and W.-Z. Zhang, *A TEM study of the crystallography of austenite precipitates in a duplex stainless steel*, *Acta Mater.* 55 (2007), pp. 6754–6764.
- [12] T.J. Headley and J.A. Brooks, *A new Bcc–Fcc orientation relationship observed between ferrite and austenite in solidification structures of steels*, *Metall. Mater. Trans. A* 33 (2002), pp. 5–15.

- [13] E.F. Monlevade and I.G.S. Falleiros, *Orientation relationships associated with austenite formation from ferrite in a coarse-grained duplex stainless steel*, Metall. Mater. Trans. A 37 (2006), pp. 939–949.
- [14] A.J.W. Menezes, H. Abreu, S. Kundu, H.K.D.H. Bhadeshia, and P.M. Kelly, *Crystallography of Widmanstätten austenite in duplex stainless steel weld metal*, Sci. Technol. Weld. Joining 14 (2009), pp. 4–10.
- [15] X. Fang, W. Yin, C. Qin, W. Wang, K.H. Lo, and C.H. Shek, *The interface character distribution of cold-rolled and annealed duplex stainless steel*, Mater. Charac. 118 (2016), pp. 397–404.
- [16] H. Beladi, V. Tari, I.B. Timokhina, P. Cizek, G.S. Rohrer, A.D. Rollett, and P.D. Hodgson, *On the crystallographic characteristics of nanobainitic steel*, Acta Mater. 127 (2017), pp. 426–437.
- [17] N. Haghdadi, P. Cizek, H. Beladi, and P.D. Hodgson, *The austenite microstructure evolution in a duplex stainless steel subjected to hot deformation*, Philos. Mag. 97 (2017), pp. 1209–1237.
- [18] E. Mahway, *OIM user's manual*, EDAX-TSL, NJ, 2005.
- [19] N. Haghdadi, P. Cizek, H. Beladi, and P.D. Hodgson, *A novel high-strain-rate ferrite dynamic softening mechanism facilitated by the interphase in the austenite/ferrite microstructure*, Acta Mater. 126 (2017), pp. 44–57.
- [20] D.M. Saylor, B.S. El-Dasher, B.L. Adams, and G.S. Rohrer, *Measuring the five-parameter grain-boundary distribution from observations of planar sections*, Metall. Mater. Trans. A 35 (2004), pp. 1981–1989.
- [21] G.S. Rohrer, D.M. Saylor, B. Dasher, B.L. Adams, A.D. Rollett, and P. Wynblatt, *The distribution of internal interfaces in polycrystals*, Z. Metallkd. 95 (2004), pp. 197–214.
- [22] K. Ameyama, G.C. Weatherly, and K.T. Aust, *A study of grain boundary nucleated widmanstätten precipitates in a two-phase stainless steel*, Acta Metal. Mater. 40 (1992), pp. 1835–1846.
- [23] T. Maki, I. Tamura, and K. Ameyama, *Morphology and crystallographic feature of intragranular gamma phase in (alpha+ gamma) two phase stainless steel*, Jpn. Instit. Met. J. 50 (1986), pp. 10–19.
- [24] M. Zaid and P.P. Bhattacharjee, *Electron backscatter diffraction study of deformation and recrystallization textures of individual phases in a cross-rolled duplex steel*, Mater. Charac. 96 (2014), pp. 263–272.
- [25] V. Muthupandi, P. Bala Srinivasan, S.K. Seshadri, and S. Sundaresan, *Effect of weld metal chemistry and heat input on the structure and properties of duplex stainless steel welds*, Mater. Sci. Eng. A 358 (2003), pp. 9–16.
- [26] H. Beladi, Q. Chao, and G.S. Rohrer, *Variant selection and intervariant crystallographic planes distribution in martensite in a Ti–6Al–4 V alloy*, Acta Mater. 80 (2014), pp. 478–489.
- [27] N. Yoshinaga, K. Kawasaki, H. Inoue, B. C. De Cooman, J. Dilewijns, *Modern LC and ULC sheet steels for cold forming: processing and properties*, in *Proceedings of the 15th Annual ACM*, Mainz, Aachen, Germany, 1998, p. 569.
- [28] G. Brückner and G. Gottstein, *Transformation textures during diffusional $\alpha \rightarrow \gamma \rightarrow \alpha$ phase transformations in ferritic steels*, ISIJ Int. 41 (2001), pp. 468–477.
- [29] I. Lischewski and G. Gottstein, *Orientation relationship during partial α - γ -phase transformation in microalloyed steels*, Mater. Sci. Forum 495–497 (2005), pp. 447–452.
- [30] I. Lischewski, D.M. Kirch, A. Ziemons, and G. Gottstein, *Investigation of the $\alpha - \gamma - \alpha$ phase transformation in steel: High-temperature in situ EBSD measurements*, Texture Stress Microstruct. 2008 (2008), pp. 1–7.
- [31] E.C. Bain, *The nature of martensite*, Trans. AIME 70 (1924), pp. 25–47.

- [32] G. Kurdjumow and G. Sachs, *On the mechanism of steel hardening*, Z. Phys. 64 (1930), pp. 325–343.
- [33] Z. Nishiyama, *X-ray investigation of the mechanism of the transformation from face centred cubic lattice to body-centred cubic*, Sci. Rep. Tôhoku Imp. Univ. 23 (1934), pp. 637–664.
- [34] W. Pitsch, *Der orientierungszusammenhang zwischen zementit und austenite*, Acta Metall. 10 (1962), pp. 897–900.
- [35] A.B. Greninger and A.R. Troiano, *The mechanism of martensite formation*, J. Met. Trans. 185 (1949), pp. 590–598.
- [36] A.F. Gourgues, H.M. Flower, and T.C. Lindley, *Electron backscattering diffraction study of acicular ferrite, bainite, and martensite steel microstructures*, Mater. Sci. Technol. 16 (2000), pp. 26–40.
- [37] Y.W. Lee and H.H. Aaronson, *Anisotropy of coherent interphase boundary energy*, Acta Metall. 28 (1980), pp. 539–548.
- [38] Y. Adachi, K. Hakata, and K. Tsuzaki, *Crystallographic analysis of grain boundary Bcc-precipitates in a Ni–Cr alloy by FESEM/EBSD and TEM/Kikuchi line methods*, Mater. Sci. Eng. A 412 (2005), pp. 252–263.
- [39] W.B. Hutchinson, L. Ryde, and P.S. Bate, *Transformation Textures in Steels*, Mater. Sci. Forum 495–497 (2005), pp. 1141–1150.
- [40] H. Beladi, N.T. Nuhfer, and G.S. Rohrer, *The five-parameter grain boundary character and energy distributions of a fully austenitic high-manganese steel using three dimensional data*, Acta Mater. 70 (2014), pp. 281–289.
- [41] D.M. Saylor, B.S. El Dasher, A.D. Rollett, and G.S. Rohrer, *Distribution of grain boundaries in aluminum as a function of five macroscopic parameters*, Acta Mater 52 (2004), pp. 3649–3655.
- [42] V. Randle, G.S. Rohrer, H.M. Miller, M. Coleman, and G.T. Owen, *Five-parameter grain boundary distribution of commercially grain boundary engineered nickel and copper*, Acta Mater. 56 (2008), pp. 2363–2373.
- [43] H. Beladi and G.S. Rohrer, *The role of thermomechanical routes on the distribution of grain boundary and interface plane orientations in transformed microstructures*, Metall. Mater. Trans. A 48 (2017), pp. 2781–2790.
- [44] H. Beladi and G.S. Rohrer, *The relative grain boundary area and energy distributions in a ferritic steel determined from three-dimensional electron backscatter diffraction maps*, Acta Mater. 61 (2013), pp. 1404–1412.
- [45] R.G. Hoagland, R.J. Kurtz, and C.H. Henager, *Slip resistance of interfaces and the strength of metallic multilayer composites*, Scr. Mater. 50 (2004), pp. 775–779.
- [46] J.M. Rigsbee and H.I. Aaronson, *A computer modeling study of partially coherent FCC: BCC boundaries*, Acta Metall. 27 (1979), pp. 351–363.
- [47] J.K. Mackenzie, A.J.W. Moore, and J.F. Nicholas, *Bonds broken at atomically flat crystal surfaces-I: Face-centred and body-centred cubic crystals*, J. Phys. Chem. Solids 23 (1962), pp. 185–196.
- [48] G. Miyamoto, R. Hori, B. Poorganji, and T. Furuhashi, *Crystallographic analysis of proeutectoid ferrite/austenite interface and interphase precipitation of vanadium carbide in medium-carbon steel*, Metal. Mater. Trans. A 44 (2013), pp. 3436–3443.
- [49] T. Furuhashi, T. Maki, and K. Oishi, *Interphase boundary structure with irrational orientation relationship formed in grain boundary precipitation*, Metal. Mater. Trans. A 33 (2002), pp. 2327–2335.
- [50] Q. Liang and W.T. Reynolds, *Determining interphase boundary orientations from near-coincidence sites*, Metal. Mater. Trans. A 29 (1998), pp. 2059–2072.
- [51] D.W. Kim, *Variant selection of Allotriomorphic Ferrite in Steels*, PhD thesis, Pohang University of Science and Technology, Korea, 2011.

- [52] T. Watanabe, *Observations of plane-matching grain boundaries by electron channelling patterns*, *Philos. Mag. A* 47 (1983), pp. 141–146.
- [53] J.J. Jonas, Y. He, and G. Langelaan, *The rotation axes and angles involved in the formation of self-accommodating plates of Widmanstätten ferrite*, *Acta Mater* 72 (2014), pp. 13–21.
- [54] O. Hellwig, K. Theis-Bröhl, G. Wilhelmi, and H. Zabel, *Growth of fcc (1 1 1) on bcc (1 1 0): Influence of growth and annealing temperature on epitaxy and surface morphology for Pd on Cr*, *Surface Sci.* 410 (1998), pp. 362–367.
- [55] G.C. Weatherly and W.-Z. Zhang, *The invariant line and precipitate morphology in Fcc–Bcc systems*, *Metall. Mater. Trans. A* 25 (1994), pp. 1865–1874.
- [56] M. El Hajjaji, *Caractérisation et simulation des joints de phases C. C. -C. F. C. : applications à des alliages Fe-Cr-Ni de différentes puretés*, *Thèse de Doctorat d'Etat*, Université Claude Bernard-Lyon I, 1986.
- [57] D.G. Brandon, *The structure of high-angle grain boundaries*, *Acta Metall.* 14 (1966), pp. 1479–1484.
- [58] A. Khorashadizadeh, D. Raabe, S. Zaeferrer, G.S. Rohrer, A.D. Rollett, and M. Winning, *Five-parameter grain boundary analysis by 3D EBSD of an ultra fine grained CuZr alloy processed by equal channel angular pressing*, *Adv. Eng. Mater.* 13 (2011), pp. 237–244.
- [59] J. Li, S.J. Dillon, and G.S. Rohrer, *Relative grain boundary area and energy distributions in nickel*, *Acta Mater.* 57 (2009), pp. 4304–4311.
- [60] G.S. Rohrer, V. Randle, C.S. Kim, and Y. Hu, *Changes in the five-parameter grain boundary character distribution in α -brass brought about by iterative thermomechanical processing*, *Acta Mater.* 54 (2006), pp. 4489–4502.
- [61] H. Beladi, G.S. Rohrer, A.D. Rollett, V. Tari, and P.D. Hodgson, *The distribution of intervariant crystallographic planes in a lath martensite using five macroscopic parameters*, *Acta Mater.* 63 (2014), pp. 86–98.
- [62] B. Hutchinson, J. Komenda, G.S. Rohrer, and H. Beladi, *Heat affected zone microstructures and their influence on toughness in two microalloyed HSLA steels*, *Acta Mater.* 97 (2015), pp. 380–391.
- [63] C.S. Pande, M.A. Imam, B.B. Rath, *Study of annealing twins in FCC metals and alloys*, *Metall. Trans. A* 21 (11), pp. 2891–2896.